Characterization of a Clustering Gas Jet for High Energy Density Plasma Production

A Thesis Presented in Partial Fulfillment of the

Bachelor of Science in Physics (Dean's Scholars Honors)

and the

Bachelor of Arts in Plan II Honors

Degrees

Griffin Dale Glenn

Department of Physics

The University of Texas at Austin

20 May 2019

Professor Todd Ditmire (Supervisor)

_____

Signature

_____

Date

Professor Greg Sitz (Second Reader)

_____

Signature

_____

Date

Acknowledgments

First, I would like to thank my research advisor, Professor Todd Ditmire. His guidance has been enormously helpful throughout my undergraduate career, and I deeply appreciate his willingness to take me into his group in my freshman year. I am also grateful to other members of the Ditmire group: Andrew Yandow and Craig Wagner first introduced me to HEDS, and Gilliss Dyer provided essential mentorship when I first joined the group. I was fortunate to work with Ganesh Tiwari on two Texas Petawatt experimental campaigns, and I look forward to working on many more with Grant Richmond. Without the support and leadership of Hernan Quevedo this thesis would have been impossible, and it was a pleasure to work with Cody Chang on this project. I'd like to thank my friends, too numerous to name, who have kindly humored my drawn-out descriptions of my work in the lab. Finally, I would like to thank my family, Steve, Shannon, and Gillian Glenn, and my girlfriend Alex Miller, who have been my longest and most steadfast supporters.

Abstract

When expanding through a nozzle into a vacuum in a high-pressure-backed supersonic jet, certain gases can condense into van der Waals-bound atomic or molecular clusters. These clusters absorb intense, pulsed laser light more efficiently than uniform gas jets of the same average density, making them useful sources of high energy density plasmas. An argon gas jet designed to produce such clusters was studied using Rayleigh scattering and interferometry.

Contents

1 Background

1.1 Gas-Phase Clusters

Gas clusters lie in between the highly distinct regimes occupied by single atoms or molecules and condensed matter states, and are typically composed of between 2 and 10^4 monomers held together by hydrogen bonding or van der Waals forces(1; 2). The stark difference between the average density of a jet of gas clusters and the local density of individual clusters contributes to often-unexpected behavior that has found applications in a variety of settings. These applications range from the generation of energetic x-rays and ions to the demonstration of D-D fusion(3; 4; 5). Gas clusters have also been observed to absorb short-pulse laser light highly efficiently, making them particularly useful as a tabletop source of high-temperature plasmas(6).

One method of producing such clusters that particularly lends itself to the production of clusters of alkali metals is to use an oven in conjunction with a skimmer and condenser(7). Clusters composed of gases such as Ar, Xe, Kr, N_2, and CO_2 can be effectively produced by allowing a supersonic jet of the gas to expand into vacuum(1; 2). In this case, the cooling experienced in the frame of the expanding gas causes the formation of clusters in the jet. These clusters can serve as nucleation sites for the production of still-larger clusters up to about 10^4 atoms or molecules(8). The sizes of the clusters are distributed log-normally, so clusters substantially larger than the average will be present in the gas jet in non-negligible quantities(9).

$$\Gamma^* = \frac{k\left(d/\tan(\alpha)\right)^{0.85}}{T_0^{2.29}} P_0 \tag{1}$$

The clustering process is conventionally described by the Hagena parameter, denoted Γ^*(1; 2). This parameter is given by Eq. 1, where d is the nozzle diameter in mm, α is the opening half-angle of the nozzle ($< 45°$ for a supersonic nozzle), T_0 is the temperature of the backing gas, P_0 is the pressure of the backing gas, and k is a gas-dependent constant. For Ar, $k = 1650$, whereas for N_2, $k = 528$(10). Cluster formation typically begins when Γ^* is of order 10^2, at which point the number of monomers per cluster N_c scales as $(\Gamma^*)^{2.0-2.5}$(10).

1.2 Clustering Gas Jet

The gas jets employed to produce gas clusters typically possess a few consistent features. A pulsed solenoid valve allows the nozzle to open for times of order 1 ms against the backing pressure of the gas. The temperature of the backing gas is an important parameter to track and control, and the use of a cooling jacket surrounding the valve allows this to be accomplished. The use of an indium seal enables cryogenic operation while still granting some flexibility in valve assembly to optimize its operation(10). A schematic

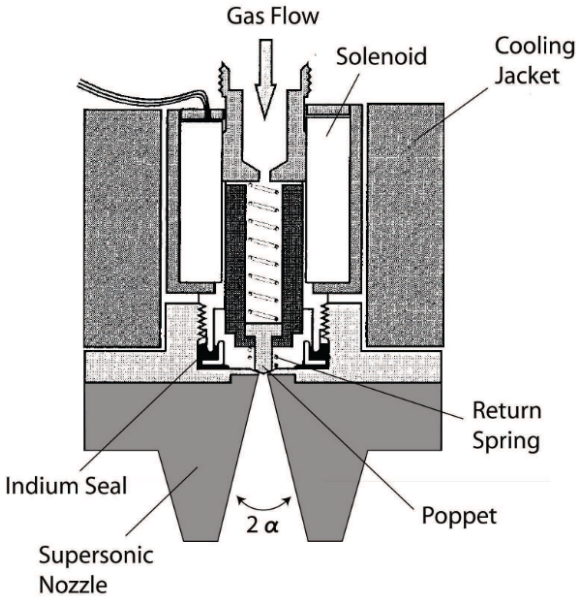

Figure 1: This is a schematic of a typical gas jet used to produce gas clusters at either room temperature or cryogenic temperatures. Figure courtesy of Ref. 11; originally adapted from Ref. 10.

of such a jet is presented in Fig. 1.

1.3 Gas Jet Characterization Methods

A variety of methods have been used to characterize the clusters produced by supersonic gas jets. Illuminating the cluster jet and capturing Rayleigh-scattered light is a useful method of verifying the formation of clusters, but provides insufficient information to determine the average cluster size without additional information about the cluster density. A variety of other experimental approaches have been used to measure the average cluster size, but many of them require the use of sophisticated additional instrumentation and rely on fragmenting the clusters, complicating data analysis(12).

By supplementing Rayleigh scattering with interferometry of the neutral cluster jet, both the average cluster size and the average density of clusters can be obtained(12). This method is all-optical and can serve as a relatively straightforward addition to many experimental designs which call for a cluster jet.

1.3.1 Rayleigh Scattering

Rayleigh scattering is the elastic scattering of light by particles much smaller than its wavelength. Averaged across scattering angles, the classical Rayleigh scattering cross-section is given by Eq. 2, where r is the radius of the cluster, λ is the wavelength of the incident light, and n is the index of refraction of the medium(10). Due to the strong dependence of S_{RS} on r, we expect for Rayleigh-scattered light to only be

visible in a detector if clusters are forming.

$$S_{RS} = \frac{8\pi r^6}{3\lambda^4} \left(\frac{n^2 - 1}{n^2 + 2} \right)^2 \tag{2}$$

For spherical clusters, the scattering signal S_{RS} is proportional to the monomer density before clustering n_0 times N_c. We know that $n_0 = P_0$, and the Hagena parameter implies that $N_c \propto P_0^{2.0-2.5}$. As such, the Rayleigh-scattered signal is anticipated to vary as $P_0^{3.0-3.5}$(10).

1.3.2 Interferometry

The presence of clusters will influence the refractive index through the jet. The change in radial refractive index $\Delta n_r(x)$ is given (again neglecting contributions from monomers) by $2\pi\gamma N_c$, where γ is the cluster polarizability. It can be shown that

$$\overline{r^3} N_c = \frac{\Delta n_r(x)}{2\pi} \left(\frac{\epsilon + 2}{\epsilon + 1} \right), \tag{3}$$

where $\overline{r^3}$ is averaged over the cluster size distribution and ϵ is the dielectric function of the bulk material within the cluster(12). By complementing measurements of Rayleigh scattering with a measurement of $\Delta n_r(x)$, both the effective radius and the density of the gas clusters can be obtained.

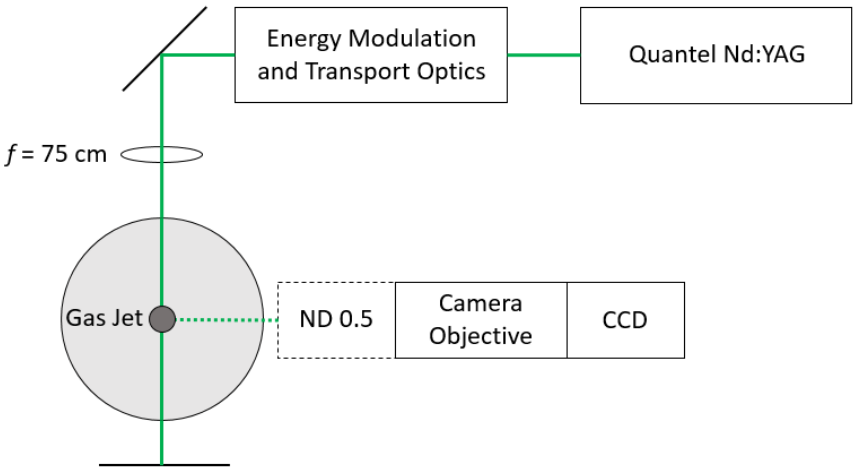

Figure 2: A top-down schematic of the Rayleigh scattering setup. The Quantel laser passes first through a polarizing beamsplitter and a polarizer to modulate the energy. The beam is then focused into the center of the target chamber using a lens with focal length $f = 75$ cm. The Rayleigh-scattered light is collected using a camera objective (AF Micro-NIKKOR 200mm) and a Basler ace CCD camera.

2 Results

2.1 Rayleigh Scattering

We began the characterization process by seeking to observe the formation of gas clusters. This was most easily accomplished by illuminating the gas jet with a weakly focused laser beam and observing the light scattered by the gas clusters at 90° from the laser forward direction due to Rayleigh scattering.

A schematic of the Rayleigh scattering setup is shown in Fig. 2. A Quantel Brilliant Q-switched Nd:YAG laser with a 2ω attachment produced up to 150 mJ of 532 nm light in pulses of FWHM approximately 4 ns. Using a polarizing beamsplitter and a polarizer, the laser energy delivered to the chamber could be modulated from its maximum value to below 1 mJ, with the rejected laser light delivered directly to a beam dump. During both the Rayleigh scattering experiments and subsequent interferometry, the polarizer was tuned such that approximately 1 mJ of laser energy was transmitted to the target chamber. The gas jet was aligned to the center of the chamber using a pair of Thorlabs diode alignment lasers. Then, the beam from the Quantel, which had been aligned colinearly with one of the alignment beams, was focused using a converging lens with focal length $f = 75$ cm into the center of the target chamber. The Rayleigh-scattered light was collected at an angle of 90° using a camera objective (AF Micro-NIKKOR 200mm) and a Basler ace CCD camera.

All timings were governed by a Stanford Research Services DG535 timing box. First, a delay of 182 μs was established between the activation of the Quantel flashlamps and the firing of the Q-switch. This timing was established empirically by varying the timing and observing the laser energy on an Ophir Nova

II energy meter, and is also consistent with the timing described in the Quantel laser manual. To facilitate comparison with Ref. (11), the gas jet was set to open for 3 ms. The camera began to acquire data 1 ms before the opening of the valve, and the laser was fired 1 ms after that, allowing the camera to capture the complete duration of the laser pulse while minimizing background signal.

These initial studies of cluster formation were initially planned to be performed with nitrogen, but acquiring signal was challenging without increasing the laser energy to levels that risked damaging transport optics. So, the gas was changed to argon. Given the relative k-values for the two gases and the strong dependence of S_{RS} on the Hagena parameter, we expected and indeed observed a significant increase in the level of signal observed that allowed the rest of the measurements to proceed smoothly.

The pressure within the backing gas was monitored by an Omega Engineering pressure sensor. The regulator connecting the argon cylinder to the gas jet could not be opened to provide pressures above approximately 425 psi. This imposed an upper bound on the backing pressures we were able to study.

To pursue future experiments on magnetically-confined HED plasmas it will be necessary to generate clusters within the confines of a metal coil approximately 5 mm to 1 cm in diameter. In order to confirm the formation of clusters in this scenario in addition to the "empty chamber" case, Rayleigh scattering data were also collected with such coils installed. To capture the dependence of gas jet height on the cluster-forming process, data were acquired with the nozzle at multiple heights above the laser beam when possible. In all, Rayleigh scattering data were captured for the empty chamber and two nozzles at multiple heights using backing pressures that ranged from approximately 50 psi to approximately 450 psi in steps of approximately 50 psi.

2.2 Interferometry

In order to characterize changes in the index of refraction through the gas jet, the 75 cm lens from the Rayleigh scattering design was removed and a Mach-Zehnder interferometer was constructed. The final design of this interferometer is presented in Fig. 3. Beamsplitters were placed such that one leg of the Quantel beam would pass along the same path as the Rayleigh scattering design while the other leg would pass through the air adjacent to the target chamber. A second beamsplitter recombined the two legs and directed them into a separate Basler ace CCD camera.

To ensure that the camera was imaging the plane of the nozzle, the legs of the interferometer incorporated imaging telescopes. The initial design used one lens with $f = 25$ cm and two lenses with $f = 15$ cm to form a pair of beam-expanding telescopes. A sample interferogram from this design is presented in Fig. 4.

However, this design was difficult to align due to its use of one lens in two telescopes and was therefore

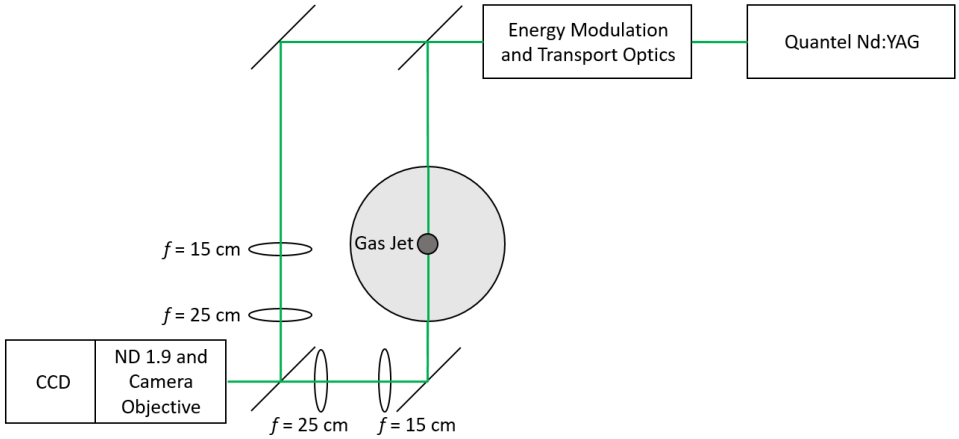

Figure 3: The final design of the interferometer.

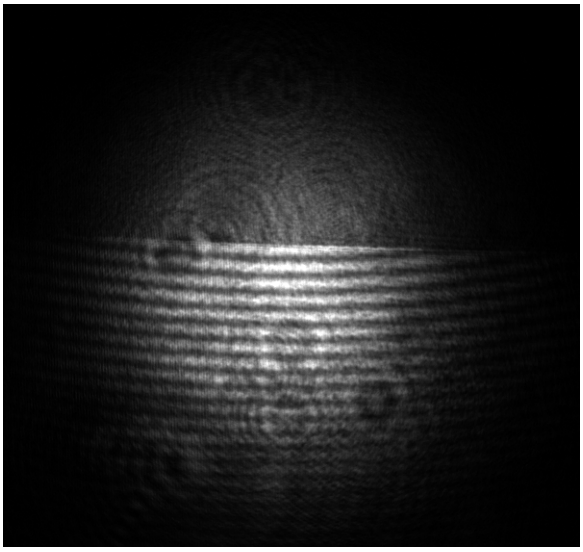

Figure 4: A sample interferogram from the initial design of the interferometer, which used three lenses to build a telescope in each leg of the interferometer. A narrowed iris provided the circular beam profile.

superseded by a second design. The second interferometer design replaced the three previous lenses with two $f = 15$ cm lenses and two $f = 25$ cm lenses, allowing a separate beam-expanding telescope to be built and independently aligned in each leg of the interferometer. A sample interferogram from this design is presented in Fig. 5.

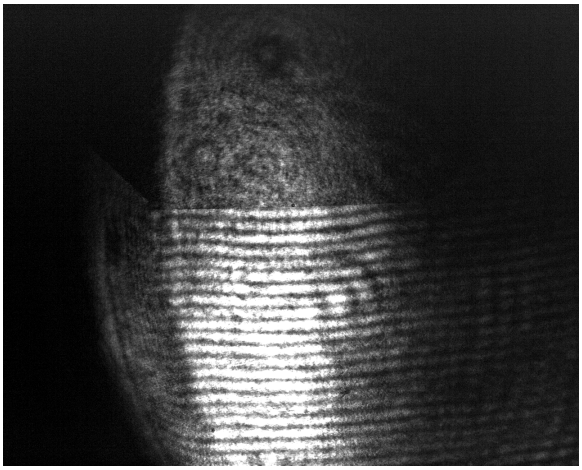

Figure 5: A sample interferogram from the second design of the interferometer. The ellipticity of the beam is the result of a poor beam profile from the Quantel. A 1-to-2 telescope will be implemented in order to alleviate this issue.

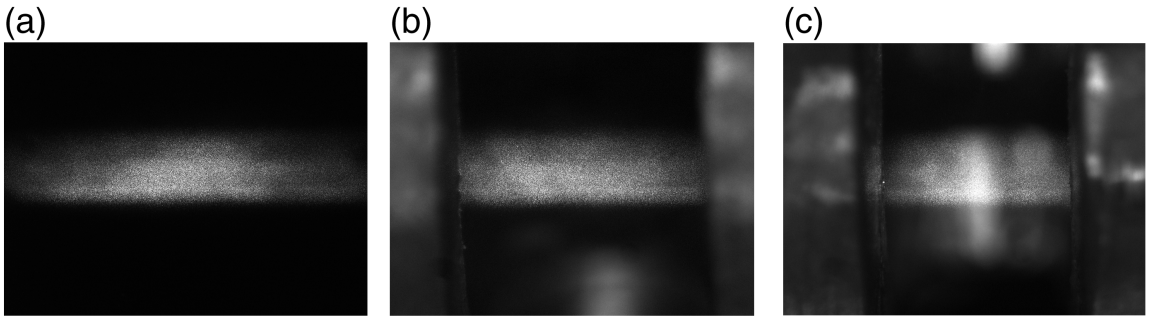

Figure 6: Clusters forming with the nozzle at a height of 10 mm above the laser beam. (a) Empty vacuum chamber. (b) Medium coil (inner diameter 13 mm). (c) Small coil (inner diameter 9 mm).

3 Discussion

3.1 Rayleigh Scattering

A nozzle height of 10 mm placed the nozzle just above the larger of the two coils tested. Fig. 6 demonstrates that, at this position, clusters were readily apparent not only using the larger coil, but also with the smaller coil and with an empty vacuum chamber.

Fig. 7 shows the results of four scans in backing pressure at four different nozzle heights above the Quantel beam with no coil installed. The three lowest positions are relatively consistent with each other and align with the findings of Refs. 12 and 11, which found a weaker dependence of S_{RS} on P_0 for argon than predicted by the Hagena parameter, indicating that this measure likely overestimates the cluster size for large clusters. At the highest nozzle position, the cluster beam had broadened enough by the time it had propagated down to the camera field of view that it is possible that scattering signal was cut off. Since the region clearly

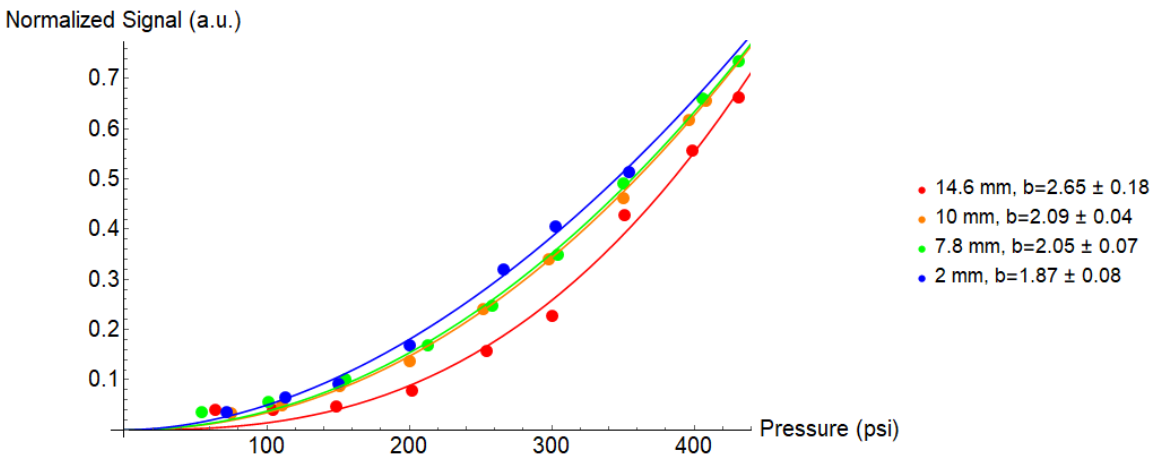

Figure 7: These fits present four scans in backing pressure at four different nozzle heights above the Quantel laser beam. No coils were installed in these tests. The data (dots) were fit (solid line) to an equation of the form $S_{RS} \propto x^b$.

scattering light grew with higher backing pressures, this effect may not have been consistent across pressures and as such could have distorted the fit.

In initial testing, clusters were even observed with the jet at a height of 7.8 mm, just above the top of the small coil, suggesting that the argon clusters were very robust against destruction due to obstructions below the nozzle. To further test the robustness of the cluster formation, Rayleigh scattering data was also captured when an upturned full-size optical baseplate was set up directly below the level of the laser. This was expected to provide a worst-case scenario for the formation of clusters, as the shock wave produced by the supersonic jet's incidence on the baseplate was anticipated to significantly disrupt cluster formation. However, even this measure did not seem to substantially disrupt the cluster formation process, as shown in Fig. 8. The unexpected robustness of these gas clusters has yet to be fully explained, and as such provides an important future direction for this project.

3.2 Interferometry

Interferograms acquired without argon and at three different backing pressures are presented in Fig. 9. These interferograms align with what we might expect, in that increasing the backing pressure leads to a greater fringe shift due to the presence of more gas in the jet. Moreover, the point of greatest fringe deflection is approximately centered on the nozzle, indicating that the setup is well-aligned and that the gas density is greatest near the center of the nozzle.

The addition of a 1-to-2 telescope to the setup prior to the interferometer in order to expand the laser beam and provide an improved field of view is currently under way. Once this step is complete, the fringe shift

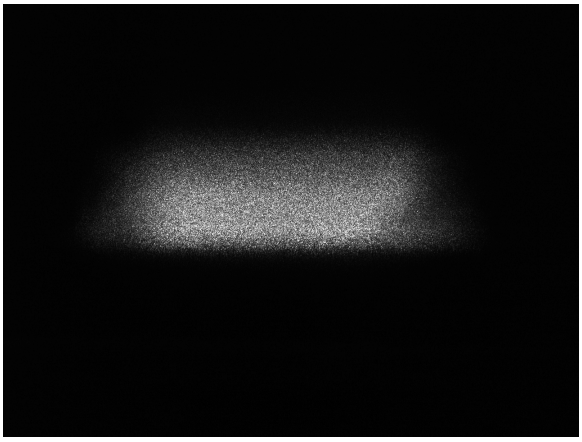

Figure 8: Image of the clusters that were seen even with the baseplate in place and the nozzle lowered to 2 mm above the beam, just out of the frame.

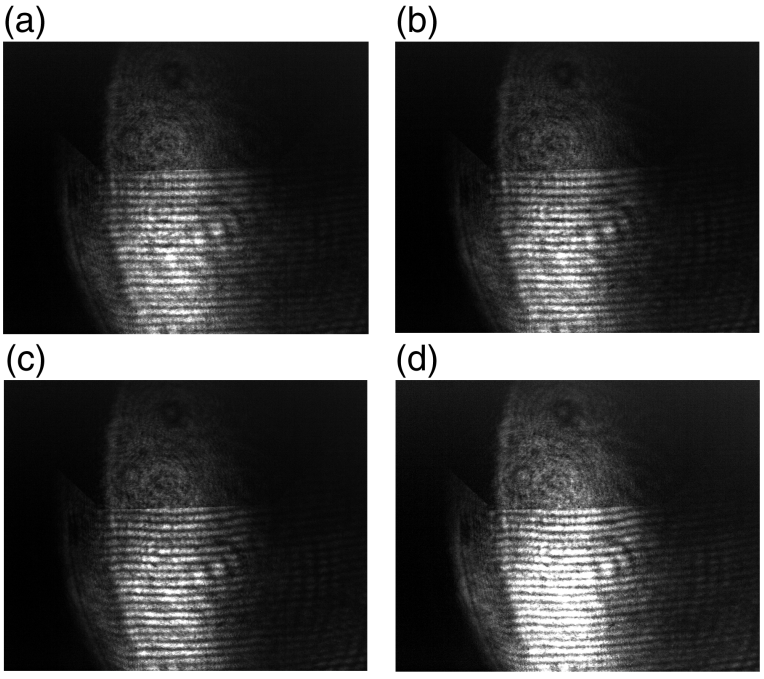

Figure 9: Interferograms acquired using the second interferometer. (a) No gas added. (b) $P_0 = 202$ psi. (c) $P_0 = 306$ psi. (d) $P_0 = 402$ psi. The progressively larger fringe shifts as a function of backing pressure suggest that higher backing pressures are associated with greater quantities of gas in the jet, as might be expected.

can be analyzed and an Abel inversion performed to extract the radial index of refraction of the clustering gas jet.

4 Conclusion

A supersonic gas jet used to produce gas clusters was studied using both Rayleigh scattering of a weakly focused laser beam and interferometry. The Rayleigh scattering signal exhibited a substantial dependence on the backing pressure of the gas, indicating that clusters were forming. The observed dependence, although weaker than predicted theoretically, was consistent with other measurements in the literature. Additional Rayleigh scattering measurements suggested that the gas clusters were unexpectedly robust against disruption. Studying this interaction in more detail will be a useful future direction for the project. Additionally, a Mach-Zehnder interferometer was built and allowed interferograms of the neutral gas jet to be obtained. Once additional improvements are completed, interferograms measuring a larger region below the gas jet nozzle can be analyzed to determine the change in the radial index of refraction created by the clustering gas jet. This will enable the determination of the pressure-dependent cluster size and number density using this nozzle, providing a firm foundation for its use in future studies of high energy density plasmas generated by high-intensity laser irradiation of these clusters.

A Development of a Magnetic Electron-Positron Spectrometer

From spring 2016 to fall 2017, a magnetic electron-positron spectrometer was designed and built. This spectrometer, known as the Global Spectrometer for Positron and Electron Characterization (GSPEC), was designed to complement the set of electron spectrometers already present in the Texas Petawatt diagnostic suite, as it was sensitive to significantly greater electron energies than the spectrometers previously in use at the TPW. This spectrometer was used to collect data in collaboration with groups from SLAC National Accelerator Laboratory and Rice University. In this appendix, which has been adapted from Ref. 13, we describe the design, construction, and simulation of the spectrometer, outline the data analysis framework used to deconvolve electron spectra from imaging plate data, and provide an example of an experimentally-obtained electron spectrum.

A.1 Operational Principle and Design

The operational principle of the GSPEC is comparable to that of other spectrometers described in the literature (14). Charged particles enter the GSPEC through a ⌀5 mm pinhole, pass through a static dipole magnetic field, and are dispersed along the walls of the spectrometer according to their energies. The GSPEC enclosure is shown in Figure 10.

The GSPEC was designed in RADIA, a 3D code that solves boundary magnetostatic problems with the boundary integral approach (15; 16). The code is optimized for use with wigglers and undulators and is available as a package for *Mathematica* (17). RADIA models the magnetic materials present in the GSPEC and computes the magnetic field for trajectories through the center of the spectrometer with a high degree of accuracy. After assembly of the spectrometer, the central magnetic field was measured using a Hall probe and found to agree well with RADIA calculations.

The GSPEC consists of two trapezoidal Ni-plated NdFeB permanent magnets. The field strength between the two magnets is 0.77 T in the center and decreases to 0.11 T at the position of the imaging plates. A yoke made of 430 stainless steel secures the magnets and confines the magnetic field. Grooves on the left, right, and back walls of the GSPEC hold the imaging plates (152 mm x 5 mm on the walls and 100 mm x 5 mm on the back) securely in place. The magnetic yoke assembly is enclosed in a custom light-tight case made of aluminum. Additionally, the back lid of the GSPEC can be easily removed to access the imaging plates after each laser shot. The interior of the GSPEC is shown in Figure 11.

The front of the GSPEC is made of 1.5"-thick lead and acetal resin that blocks x-rays from the laser-plasma interaction and secondary x-rays from energetic particles that do not enter the pinhole. The current ⌀5 mm pinhole through this shielding was chosen to balance the competing demands of improving both

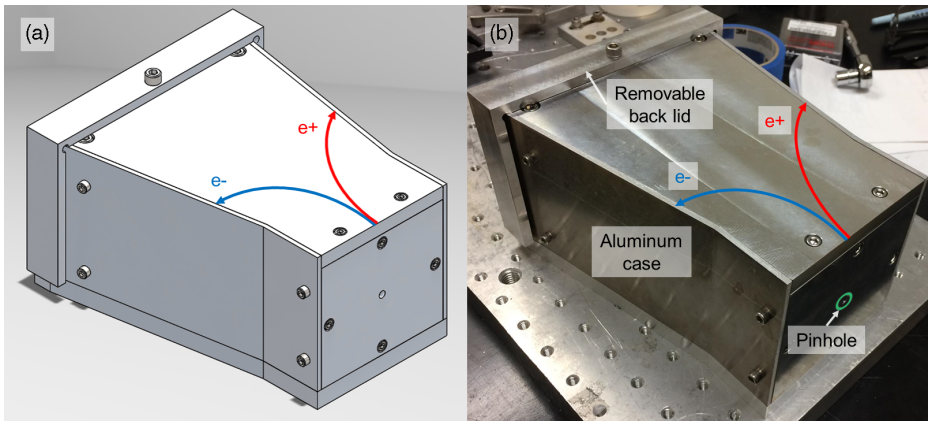

Figure 10: (a) A CAD model of the complete GSPEC assembly. (b) Following the specifications of the CAD model, the GSPEC was manufactured in the UT Austin Physics Machine Shop. The enclosure consists of a light-tight aluminum case, removable back lid, and front pinhole. In both images schematic trajectories of electrons and positrons are visible.

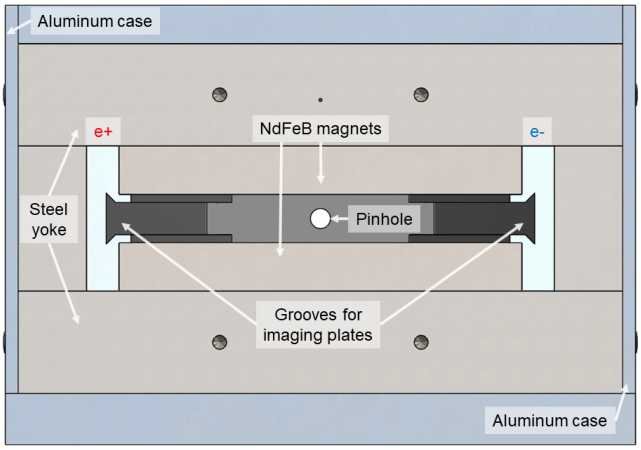

Figure 11: Rear view of the GSPEC with the back lid removed. The magnets, yoke, case, imaging plate holders, pinhole, and sides corresponding to positrons and electrons are indicated in the figure.

flux and resolution. The shielding pieces can easily be changed according to experimental needs; a smaller pinhole could be used for improved energy resolution or a larger pinhole could be used for increased signal level.

A.2 Simulation of Electron and Positron Trajectories

Once the magnetic field map inside the GSPEC was obtained with RADIA, a particle pusher code based on the Runge-Kutta-Fehlberg (RK45) method for solving ordinary differential equations was used to simulate the trajectories of electrons of various energies within the spectrometer (18). According to the simulated trajectories electrons with energies of approximately 3–50 MeV are detected on the side imaging plate, while electrons with energies greater than 60 MeV are detected on the back imaging plate. The trapezoidal magnet design used in the GSPEC maintains relatively even electron energy dispersion across the side imaging plate and focuses electron trajectories between approximately 5 and 15 MeV. These trajectories and the magnetic field computed by RADIA are displayed in Figure 12. The back imaging plate also collects an x-ray zero point, which is indistinguishable from electron signal for electron energies greater than 150 MeV. This places an upper bound on the electron energy resolvable with the GSPEC. Because it is left-right symmetric, energetic positrons can be detected on the right imaging plate with an energy resolution similar to that observed for electrons. The signal of positrons with energies greater than 60 MeV is indistinguishable from the proton signal on the back imaging plate, placing an upper bound of 50 MeV on the positron energy directly resolvable with the GSPEC.

The GSPEC compares favorably to several other spectrometers in the literature. It is sensitive to both positrons and electrons, increasing its versatility compared to electron-only spectrometers like the spectrometer mentioned in Ref. 19. It is also capable of capturing significantly higher electron energies than the spectrometers in Refs. 14 and 19, which can observe energies up to only 4 and 18 MeV respectively. As such, it is better-suited for observing the hot electrons produced in high-energy short-pulse experiments than those spectrometers. It is also more compact than the electron spectrometer described in Ref. 20, which is sensitive to an energy range similar to that captured by the GSPEC's low-energy walls. Additionally, from 5–15 MeV the GSPEC focuses electrons along the detector plane, improving its resolution in this energy range. As shown in Figure 13, the change in incident electron energy per change in distance along the IP at each point on the IP also varies more across the energy range of the spectrometer described in Ref. 20 than for the GSPEC. This means that the GSPEC has more consistent resolution with increasing energy on the low-energy walls than the spectrometer described in Ref. 20.

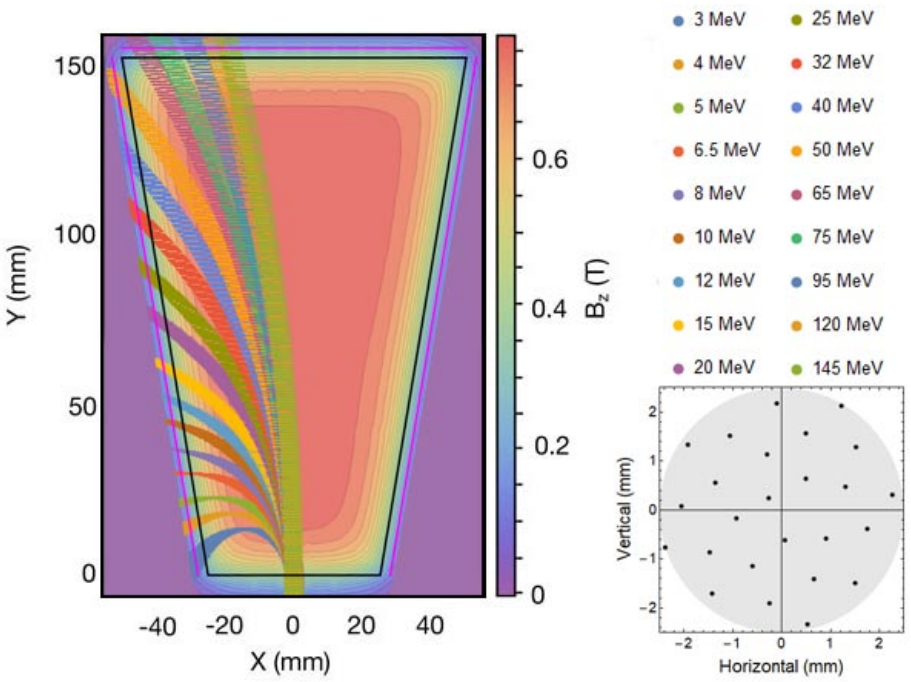

Figure 12: The magnetic field computed by RADIA in the Z=0 plane and the calculated trajectories for electrons of various energies. The electrons' initial positions (shown on the bottom right) are chosen at random from within the ⌀5 mm pinhole (shown in gray). The angular divergence of the electron beam is given by the experimental geometry. In this simulation ±5 mrad was used for consistency with the experiment described below. The field in the region to the right and left of the magnets was set to 0. Because the electrons do not pass through this region before intersecting the imaging plate its effect on their trajectories is negligible. The three imaging plates are indicated in purple. The physical separation between the side and back imaging plates results in a discontinuity in the observable electron spectrum between 50 and 60 MeV.

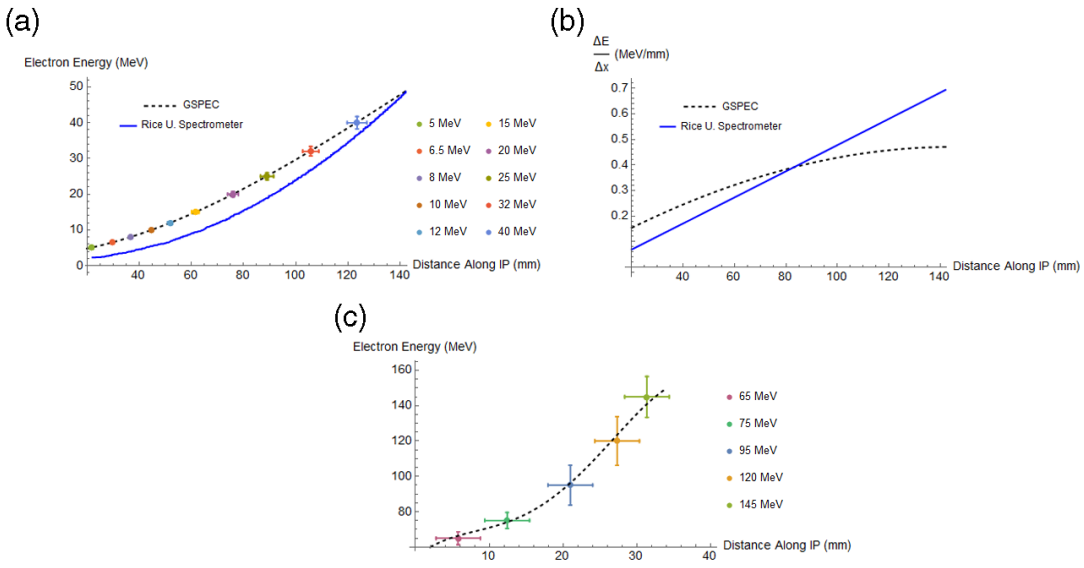

Figure 13: (a) The electron dispersion curves of the GSPEC's low energy wall and the spectrometer described in Ref. 20, with the flatter curve of the GSPEC shown. Points on the dispersion curve corresponding to particular electron energies have been plotted for the GSPEC. (b) Comparison of the change in incident electron energy per change in distance at each step along the IP for the GSPEC and the spectrometer described in Ref. 20. The flatter curve corresponding to the GSPEC indicates that its resolution is more even over the IP. It also demonstrates that the GSPEC maintains higher resolution with increasing electron energies compared to the spectrometer described in Ref. 20. (c) The electron dispersion curve of the GSPEC on the high energy back wall.

A.3 Data Analysis Framework

Raw data (photostimulated luminescence counts, or PSL) were extracted from the imaging plate via scanning with a calibrated Fuji FLA 7000 scanner (21). A background region was chosen between the electron signal and the region where the signal was blocked by the IP holder. This background region was subtracted from the signal to obtain background-free PSL counts, which were then summed to obtain the total PSL at each position along the IP. IP positions were transformed to electron energies using the simulated electron trajectories. PSL values were scaled into electron numbers using data obtained from a calibrated set of IPs which describe the fading characteristics of IPs and their sensitivity to incident electron energies and angles (22). The total electron number incident on the imaging plate could then be calculated from the pinhole size. The PSL data and associated electron energy spectrum from TPW Shot #11530 onto a wire target are plotted in Figure 15.

A.4 Experimental Demonstration

The Texas Petawatt Laser (TPW) is an Nd:glass laser based on Optical Parametric Chirped Pulse Amplification that is capable of delivering a 140 J, 130 fs pulse of s-polarized laser light centered on 1057

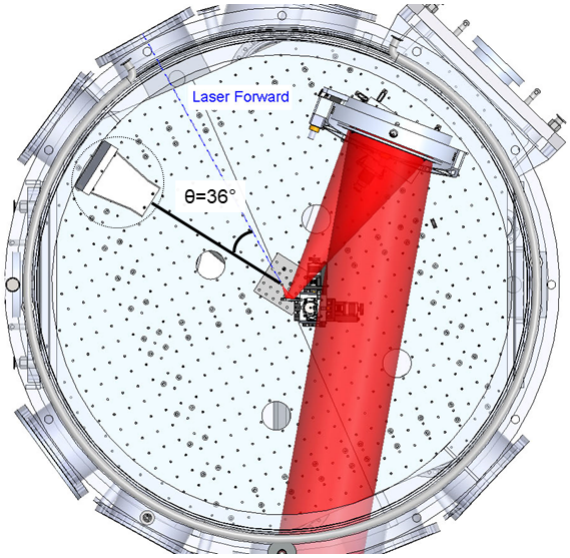

Figure 14: The top view of a CAD rendering of the GSPEC in Texas Petawatt Target Chamber 1. The path of the laser is depicted by the broad red line; the laser forward direction is indicated by the dashed blue line. The GSPEC (circled) was placed 36° azimuthally from laser forward at a declination angle of 11°.

nm (23; 24) .

Recently, a planar jet of cryogenic hydrogen was irradiated by the Texas Petawatt laser to investigate enhanced ion acceleration in the relativistic transparency regime where >100 MeV protons are predicted (25). The planar jet of cryogenic hydrogen is a continuous column with a typical rectangular geometrical cross-section of a few 10s of μm by a few μm (26). These mass-limited low-Z near-critical-density targets require ultra-high laser pulse contrast since they readily become sub-critical due to rapid expansion initiated by laser pre-pulse (27; 28). As such, the laser was focused with an f/3 off-axis parabolic mirror and contrast-enhanced using a single plasma mirror in the converging beam. The resulting on-target intensity was 1×10^{21} W/cm^2.

The GSPEC was used to capture electron spectra at a distance of 48 cm from the interaction with a horizontal offset of 36° from the laser propagation direction and a declination angle of 11°. Figure 14 shows a CAD rendering of the GSPEC's position in the target chamber. In Figure 15 we present, as a demonstration of operational principle, the electron spectrum from a vertical $\varnothing$25 μm Au wire. These wires, which are of a similar size to the hydrogen jet target, were used as surrogate targets during the experiment for diagnostic alignment and calibration purposes. The primary results of the experiment will be described in a subsequent publication.

Collisionless absorption mechanisms such as resonant absorption and vacuum heating via Brunel's mechanism are capable of producing a suprathermal tail in the energy spectrum of electrons accelerated by the interaction of an ultraintense laser with a solid target (29; 30). This tail is typically Maxwellian and can be fit to an exponential of the form $N \sim \exp(-E/kT)$ for number of electrons N, energy E, and characteristic

temperature kT (20). As seen in Figure 15, for TPW Shot #11530 the fit indicates that the characteristic temperature of this tail is approximately 1.74 MeV.

This temperature is reasonably close to the temperature predicted by the model proposed by Haines et al., which is given by Eq. 4 (31). I_{18} is the laser intensity in units of 10^{18} W/cm^2.

$$T_{e,hot}\ [\text{keV}] = m_e c^2 \left(\sqrt{1 + a_0 \sqrt{2}} - 1 \right) \cong 511 \ \left(\sqrt{1 + 1.2 \sqrt{I_{18} \lambda_{0,\mu\text{m}}^2}} - 1 \right) \tag{4}$$

The dimensionless magnetic potential a_0 is related to the laser intensity I by

$$I = \frac{2\pi^2 m_e^2 c^3 a_0^2}{\mu_0 e^2 \lambda^2},$$

where λ is the vacuum laser wavelength. When evaluated at the experimental laser intensity of approximately 1×10^{21} W/cm^2 after a single plasma mirror, this model suggests a hot-electron temperature of 2.78 MeV, in fair agreement with the hot electron temperature of 1.74 MeV obtained using the GSPEC. The difference between the two temperatures likely stems from the fact that the experimental target thickness of 25 μm was significantly larger than the thickness of a few skin depths used in Ref. 31 to develop the model.

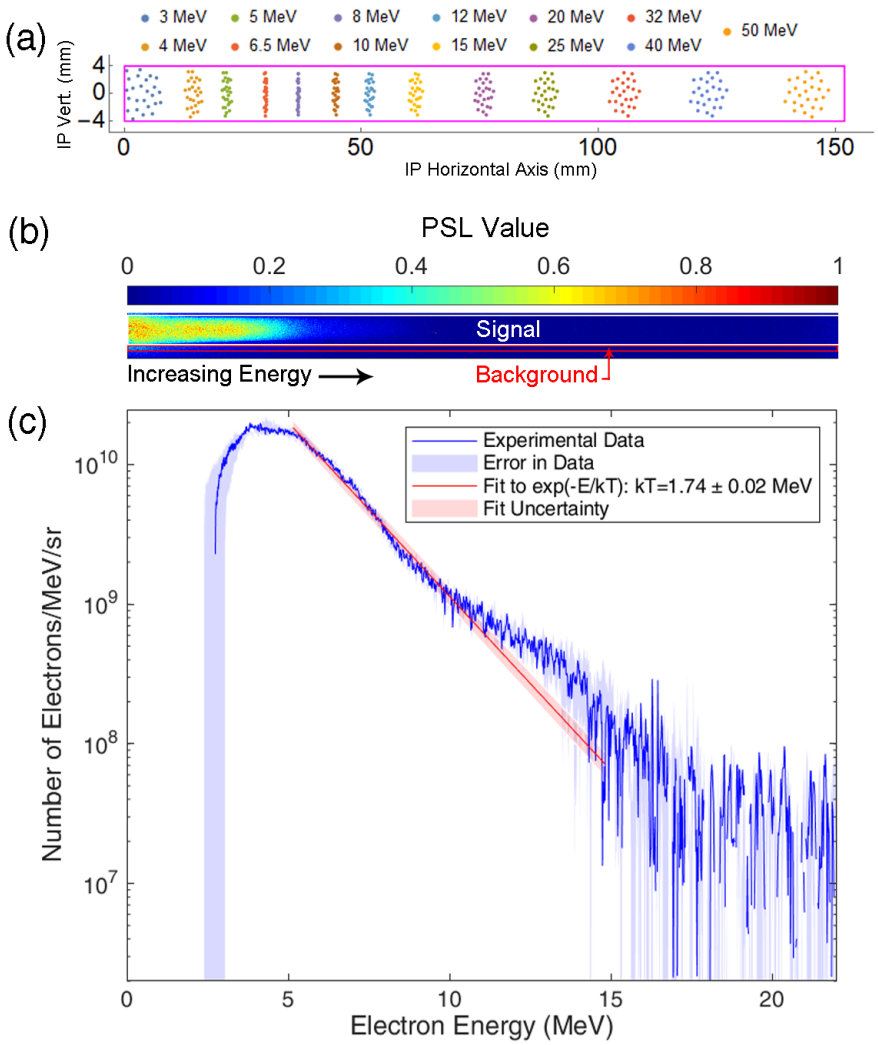

Figure 15: (a) The simulated intersections of electron trajectories with the left wall imaging plate for several electron energies. (b) The PSL data collected from the left wall imaging plate after the interaction of a Texas Petawatt laser pulse with intensity 1×10^{21} W/cm^2 and a $\varnothing 25$ μm gold wire. (c) The electron spectrum obtained from (b), with an effective temperature of 1.74 MeV. The error bar on the electron spectrum comes from both the imaging plate and the size of the pinhole.

References

[1] O. F. Hagena and W. Obert, "Cluster formation in expanding supersonic jets: effect of pressure, temperature, nozzle size, and test gas," *The Journal of Chemical Physics*, vol. 56, no. 5, pp. 1793–1802, 1972.

[2] O. F. Hagena, "Cluster ion sources (invited)," *Review of Scientific Instruments*, vol. 63, no. 4, pp. 2374–2379, 1992.

[3] A. McPherson, T. S. Luk, B. D. Thompson, A. B. Borisov, O. B. Shiryaev, X. Chen, K. Boyer, and C. K. Rhodes, "Multiphoton induced x-ray emission from Kr clusters on M-shell (100) and L-shell (6) transitions," *Physical Review Letters*, vol. 72, no. 12, pp. 1810–1813, 1994.

[4] T. Ditmire, J. W. Tisch, E. Springate, M. B. Mason, N. Hay, R. A. Smith, J. Marangos, and M. H. Hutchinson, "High-energy ions produced in explosions of superheated atomic clusters," *Nature*, vol. 386, no. 6620, pp. 54–56, 1997.

[5] T. Ditmire, J. Zweiback, V. P. Yanovsky, T. E. Cowan, G. Hays, and K. B. Wharton, "Nuclear fusion in gases of deuterium clusters heated with a femtosecond laser," *Physics of Plasmas*, vol. 7, no. 5, pp. 1993–1998, 2000.

[6] T. Ditmire, R. A. Smith, J. W. Tisch, and M. H. Hutchinson, "High Intensity Laser Absorption by Gases of Atomic Clusters," *Physical Review Letters*, vol. 78, no. 16, pp. 3121–3124, 1997.

[7] L. Bewig, U. Buck, C. Mehlmann, and M. Winter, "Seeded supersonic alkali cluster beam source with refilling system," *Review of Scientific Instruments*, vol. 63, no. 8, pp. 3936–3938, 1992.

[8] T. Ditmire, T. Donnelly, A. M. Rubenchik, R. W. Falcone, and M. D. Perry, "Interaction of intense laser pulses with atomic clusters," *Physical Review A*, vol. 53, no. 5, 1996.

[9] A. V. Arefiev, X. Gao, M. R. Tushentsov, X. Wang, B. Shim, B. N. Breizman, and M. C. Downer, "Size distribution and mass fraction of microclusters in laser-irradiated plasmas," *High Energy Density Physics*, vol. 6, no. 2, pp. 121–127, 2010.

[10] R. A. Smith, T. Ditmire, and J. W. Tisch, "Characterization of a cryogenically cooled high-pressure gas jet for laser/cluster interaction experiments," *Review of Scientific Instruments*, vol. 69, no. 11, pp. 3798–3804, 1998.

[11] A. F. Henig, "Ultrafast Dynamics in Explosions of Atomic Clusters Irradiated by Ultra-High Intensity Laser Pulses," Master's thesis, The University of Texas at Austin, 2005.

[12] K. Y. Kim, V. Kumarappan, and H. M. Milchberg, "Measurement of the average size and density of clusters in a gas jet," *Applied Physics Letters*, vol. 83, no. 15, pp. 3210–3212, 2003.

[13] G. Glenn, G. Tiwari, G. Dyer, C. Curry, M. Donovan, E. Gaul, M. Gauthier, S. Glenzer, J. Gordon, B. Hegelich, M. Martinez, E. McCary, M. Spinks, and T. Ditmire, "Improved large-energy-range magnetic electron-positron spectrometer for experiments with the Texas Petawatt Laser," *Journal of Instrumentation*, vol. 14, no. 03, pp. P03012–P03012, 2019.

[14] H. Chen, A. J. Link, R. Van Maren, P. K. Patel, R. Shepherd, S. C. Wilks, and P. Beiersdorfer, "High performance compact magnetic spectrometers for energetic ion and electron measurement in ultraintense short pulse laser solid interactions," *Review of Scientific Instruments*, vol. 79, no. 10, pp. 1–4, 2008.

[15] O. Chubar, P. Elleaume, and J. Chavanne, "A three-dimensional magnetostatics computer code for insertion devices," *Journal of Synchrotron Radiation*, vol. 5, pp. 481–484, 1998.

[16] P. Elleaume, O. Chubar, and J. Chavanne, "Computing 3D magnetic fields from insertion devices," in *Proceedings of the 1997 Particle Accelerator Conference*, vol. 3, pp. 3509–3511, 1998.

[17] Wolfram Research Inc., *Mathematica*. Champaign, Illinois: Wolfram Research, Inc., version 11 ed., 2018.

[18] E. Fehlberg, "Low-order classical Runge-Kutta formulas with stepsize control and their application to some heat transfer problems," tech. rep., National Aeronautics and Space Administration, Marshall, Alabama, 1969.

[19] I. Pomerantz, E. McCary, A. R. Meadows, A. Arefiev, A. C. Bernstein, C. Chester, J. Cortez, M. E. Donovan, G. Dyer, E. W. Gaul, D. Hamilton, D. Kuk, A. C. Lestrade, C. Wang, T. Ditmire, and B. M. Hegelich, "Ultrashort pulsed neutron source," *Physical Review Letters*, vol. 113, no. 18, 2014.

[20] D. Taylor, E. Liang, T. Clarke, A. Henderson, P. Chaguine, X. Wang, G. Dyer, K. Serratto, N. Riley, M. Donovan, and T. Ditmire, "Hot electron production using the Texas Petawatt Laser irradiating thick gold targets," *High Energy Density Physics*, vol. 9, no. 2, pp. 363–368, 2013.

[21] G. J. Williams, B. R. Maddox, H. Chen, S. Kojima, and M. Millecchia, "Calibration and equivalency analysis of image plate scanners," *Review of Scientific Instruments*, vol. 85, no. 11, 2014.

[22] K. A. Tanaka, T. Yabuuchi, T. Sato, R. Kodama, Y. Kitagawa, T. Takahashi, T. Ikeda, Y. Honda, and S. Okuda, "Calibration of imaging plate for high energy electron spectrometer," *Review of Scientific Instruments*, vol. 76, no. 1, p. 013507, 2005.

[23] M. Martinez, W. Bang, G. Dyer, X. Wang, E. Gaul, T. Borger, M. Ringuette, M. Spinks, H. Quevedo, A. Bernstein, M. Donovan, and T. Ditmire, "The Texas petawatt laser and current experiments," in *AIP Conference Proceedings*, vol. 1507, pp. 874–878, 2012.

[24] E. Gaul, T. Toncian, M. Martinez, J. Gordon, M. Spinks, G. Dyer, N. Truong, C. Wagner, G. Tiwari, M. E. Donovan, T. Ditmire, and B. M. Hegelich, "Improved pulse contrast on the Texas Petawatt Laser," in *Journal of Physics: Conference Series*, vol. 717, 2016.

[25] R. Mishra, F. Fiuza, and S. Glenzer, "Enhanced ion acceleration in transition from opaque to transparent plasmas," *New Journal of Physics*, vol. 20, no. 4, 2018.

[26] J. B. Kim, S. Göde, and S. H. Glenzer, "Development of a cryogenic hydrogen microjet for high-intensity, high-repetition rate experiments," *Review of Scientific Instruments*, vol. 87, 2016.

[27] L. Obst, S. Göde, M. Rehwald, F.-E. Brack, J. Branco, S. Bock, M. Bussmann, T. E. Cowan, C. B. Curry, F. Fiuza, M. Gauthier, R. Gebhardt, U. Helbig, A. Huebl, U. Hübner, A. Irman, L. Kazak, J. B. Kim, T. Kluge, S. Kraft, M. Loeser, J. Metzkes, R. Mishra, C. Rödel, H.-P. Schlenvoigt, M. Siebold, J. Tiggesbäumker, S. Wolter, T. Ziegler, U. Schramm, S. H. Glenzer, and K. Zeil, "Efficient laser-driven proton acceleration from cylindrical and planar cryogenic hydrogen jets," *Scientific Reports*, vol. 7, dec 2017.

[28] S. Göde, C. Rödel, K. Zeil, R. Mishra, M. Gauthier, F. E. Brack, T. Kluge, M. J. Macdonald, J. Metzkes, L. Obst, M. Rehwald, C. Ruyer, H. P. Schlenvoigt, W. Schumaker, P. Sommer, T. E. Cowan, U. Schramm, S. Glenzer, and F. Fiuza, "Relativistic Electron Streaming Instabilities Modulate Proton Beams Accelerated in Laser-Plasma Interactions," *Physical Review Letters*, vol. 118, no. 19, 2017.

[29] S. C. Wilks, W. L. Kruer, M. Tabak, and A. B. Langdon, "Absorption of ultra-intense laser pulses," *Physical Review Letters*, vol. 69, no. 9, pp. 1383–1386, 1992.

[30] F. Brunel, "Not-so-resonant, resonant absorption," *Physical Review Letters*, vol. 59, no. 1, pp. 52–55, 1987.

[31] M. G. Haines, M. S. Wei, F. N. Beg, and R. B. Stephens, "Hot-electron temperature and laser-light absorption in fast ignition," *Physical Review Letters*, vol. 102, no. 4, 2009.

Biography

Griffin Glenn was born in League City, Texas on November 17$^{\text{th}}$, 1996 and lived there until moving to Austin in 2015 to attend The University of Texas at Austin. At UT Austin he majored in Physics and Plan II Honors. Mr. Glenn was an active member of the College of Natural Sciences' Dean's Scholars Honors Program, serving as Council Chair from 2017–2018. He also played double bass in the UT University Orchestra. He graduated as a College of Natural Sciences Dean's Honored Graduate in May 2019 with a Bachelor of Science in Physics Honors and a Bachelor of Arts in Plan II Honors (highest honors). In September 2019 he plans to begin a PhD in Applied Physics at Stanford University with the support of a Natural Science Foundation Graduate Research Fellowship.